INTERNATIONAL JOURNAL FOR NUMERICAL METHODS IN FLUIDS, VOL. 25, 1163–1184 (1997)

ON THE ACCURACY OF THE DESINGULARIZED BOUNDARY INTEGRAL METHOD IN FREE SURFACE FLOW PROBLEMS

F. LALLI*

INSEAN, Italian Ship Model Basin, Via di Vallerano 139, I-00128 Roma, Italy

SUMMARY

In this paper the numerical properties of the desingularized boundary integral formulation were studied within the framework of free surface potential problems. Several numerical experiments were carried out on simple test cases in order to investigate the effects on the accuracy of the distance between the singularity sheet and the free boundary. The optimum value of this distance was related to the mesh size by simple correlations. Once the desingularized boundary integral formulation had been so calibrated, it was implemented for the solution of two typical free surface flow problems: wave diffraction around a fixed obstacle and wave resistance of submerged bodies. Numerical results are discussed in comparison with experimental data; the computational efficiency and accuracy of desingularized algorithms are confirmed and specified © 1977 John Wiley & Sons, Ltd.

Int. J. Numer. Meth. Fluids, **25**: 1163–1184 (1997)

No. of Figures: 14. No. of Tables: 0. No. of References: 16.

KEY WORDS: free surface flow; desingularization techniques; non-linear waves

1. INTRODUCTION

The numerical solution of free surface flow problems (e.g. wave diffraction around structures or ship wave resistance) requires the use of accurate and efficient algorithms suitable for the severe non-linear behaviour of boundary conditions at the water–air interface. In the framework of irrotational flows the fluid velocity can be expressed by means of the simple layer potential, giving rise to boundary integral methods that are powerful techniques for solving linear boundary value problems. The problem is therefore reformulated in terms of an integral equation on the boundary: the effective dimension of the problem is reduced by one and the computational domain becomes the enclosing boundary. These methods are based on a fundamental solution satisfying the differential equation (in some cases, also part of boundary conditions). In conventional boundary integral formulations the singularities of the fundamental solution lie on the problem domain boundary. This requires accurate evaluation of singular integrals, namely numerical implementation of complicated and time-consuming algorithms.

On the other hand, the use of an efficient method is the main point in non-linear free surface flow computations, since a boundary integral problem has to be solved at each time step in time-dependent problems (or, in steady problems, at each step of the iterative algorithm).

Correspondence to: F. Lalli, INSEAN, Italian Ship Model Basin, Via di Vallerano 139, I-00128 Roma, Italy.

Contract grant sponsor: Italian Ministero dei Transporti e della Navigazione; Contract grant number: INSEAN 1994-96

CCC 0271–2091/97/101163–22 $17.50

Received May 1996
Revised February 1997

Remarkable advantages such as high accuracy and simple and fast computation of influence matrices can be achieved by the desingularized element method (DEM), namely by boundary integral equations in which the singularity of the fundamental solution is placed away from the boundary.

Another meaningful feature of desingularized boundary integral equations is pointed out by Patterson and Sheikh,[1] who claim the capability of the method to 'tolerate higher-order singularities'. Moroever, in conventional boundary element methods (BEMs) the pressure and velocity on the boundary can be evaluated only at control points, whereas if a desingularized method is used, the velocities are continuous and smooth in the neighbourhood of boundaries and the streamlines around bodies can be computed more accurately.

Several papers concerned with desingularization techniques can be found in the literature.[2–8] In particular, Webster[2] concludes his work, related to the computation of potential flow around arbitrary 3D bodies, with this comment: 'submergence of the singularity sheet below the surface of the body appears to improve greatly the accuracy, as long as the sheet is not submerged too far'. Cao *et al.*[5] confirm this property in applications with boundaries extending to infinity and, moreover, observe that desingularized methods allow the use of simple numerical quadrature for the computation of influence matrices if the distance between the source point and the collocation point is sufficiently large, thus reducing the computational effort. They also observe the indirect non-singular method to be more efficient than the direct one. This result is interesting, since in free surface flows, particularly in the wave resistance problem, indirect methods are generally preferred.[3,6–10] In fact, an advantage of the indirect method is that the derivatives of the velocity potential can be obtained directly once the strength of the singularity distribution is known, while the direct method requires numerical differentiation to obtain tangential velocities.

On the other hand, it is known that the position of the singularity sheet has a deep influence on the accuracy of the solution. The optimum desingularization distance has to be chosen carefully, because if the singularities lie too close to the boundary, the solution may be inaccurate, whereas if the singularities are too far from the boundary, the linear system will be poorly conditioned.

This aspect has been analysed by Webster[2] for the computation of potential flow past arbitrary 3D bodies. He remarks that sometimes, even though for a first increase in the number of elements an improvement in the flow field accuracy is obtained, when the elements are very closely spaced, a further mesh refinement can lead to a worsening of the accuracy. This difficulty can be experienced, for instance, in determining the flow around a prolate spheroid, when the singularity surface submerged within the body does not include its foci, since there is no way to continue the solution analytically from the discretized surface to the body surface. Therefore no singularity distribution exists on this surface which will be able to generate the body. Webster observes that this kind of difficulty can be overcome by introducing suitable criteria for the choice of desingularization distance: the singularity sheet must be submerged no more than either half of a typical side of the local element or half of the local minimum curvature radius. As a result, a smaller submergence must be used for finer grids.

Cao *et al.*[5] also discuss strategies for choosing the desingularization distance and suggest this distance to be related to the local mesh size by means of a simple correlation: again they find that as the mesh becomes finer, the singularity sheet must approach the boundary. They conclude that 'accurate solutions can be obtained by the desingularized boundary method for a large range of desingularization distance of the order of the mesh size'.

Unfortunately, as experienced in the present work, this range can be different from case to case. The problem of accuracy dependence on desingularization distance has therefore been re-examined carefully. Heuristic criteria are suggested to select the position of the singularity sheet in order to minimize the error. Simple cases of wavy flows have been studied, for which the exact solution is known, in order to obtain simple correlations for the optimum value of the source location versus the

discretization parameters, similar to the one proposed by Cao *et al.*[5] The high accuracy of the desingularized method, previously detected by other authors, is shown and specified, in comparison with a conventional piecewise constant panel method.

Then this methodology has been applied for some computations concerning the non-linear diffraction of regular waves around a fixed obstacle as well as the wave resistance problem of simple-shaped submerged bodies. Grid dependence tests show a very fast convergence of the solution, in good agreement with experimental data.

2. FREE SURFACE FLOW MODEL

The free surface flow around a simple-shaped submerged body B is considered, assuming viscous and compressibility effects to be negligible. Vorticity is neither produced nor shed at the boundaries. The flow is therefore potential and the velocity field can be described by means of a harmonic function ϕ such that

$$\vec{u}(x, y, z, t) = \{u, v, w\} = \nabla\phi(x, y, z, t). \tag{1}$$

The reference frame is assumed to be fixed with the body, the x-axis is oriented as the incoming flow (incident wave train or uniform stream) and the z-axis is oriented upwards.

The boundary condition on the body surface (and at the bottom in finite depth problems) is

$$\nabla\phi \cdot \vec{n} = \frac{\partial\phi}{\partial n} = 0 \quad \text{on } \partial B, \tag{2}$$

$\vec{n}$ being the unit vector orthogonal to the solid surfaces.

The boundary conditions at the water–air interface S are more complex, since they are non-linear and to be enforced at a free boundary whose shape is not known *a priori*. The free surface can be described, when overturning of waves is excluded, by a single value function $z = \eta(x, y, t)$. This function must satisfy the kinematic condition

$$\frac{\partial\eta}{\partial t} + n\frac{\partial\eta}{\partial x} + v\frac{\partial\eta}{\partial y} = w \quad \text{on } S \tag{3}$$

and the dynamic condition for the pressure p that reads, if surface tension is neglected,

$$p = p_{\text{at}} \quad \text{on } S, \tag{4}$$

where p_{at} is the atmospheric pressure at the free surface. This condition can be related to the potential ϕ by means of Bernoulli's theorem as

$$\frac{\partial\phi}{\partial t} + \tfrac{1}{2}\nabla\phi \cdot \nabla\phi + g\eta = 0 \quad \text{on } S, \tag{5}$$

g being the acceleration due to gravity.

The problem stated in these terms does not determine a unique solution. In fact, initial conditions for the potential as well as for the free surface configuration are required, whereas in the steady case a radiation condition is to be enforced.

In all the problems studied, the symmetry condition has been fulfilled on $y = 0$ by the method of images, so only one half of the free surface has been discretized.

2.1. Unsteady flow (diffraction problem)

For computational purposes it is suitable to split the velocity potential ϕ as

$$\phi = \varphi_0 + \varphi_1, \tag{6}$$

where φ_0 is the incident wave potential (usually a Stokes wave). The convenience of expressing the potential as a sum of two terms as in (6) has been pointed out in a previous work:[8] such a decomposition avoids the need of generating the incident wave train by means of a numerical wavemaker, with all the related difficulties for calibration; on the other hand, the damping of the outgoing signals at the boundary of the discretized free surface is simplified.

The potential φ_0 is harmonic in the domain given by the space filled with the fluid and that occupied by the body. It therefore satisfies the impermeability condition on the bottom (if present) but not on the surface of the body. For the free surface elevation we assume, according to (6),

$$\eta = \eta_0 + \eta_1, \tag{7}$$

where η_0 is the free boundary in the absence of the body (incident wave).

Of course, φ_0 verifies conditions (3) and (4) on the 'free' wave η_0. On the other hand, the perturbation potential φ_1 satisfies the solid boundary condition

$$\frac{\partial \varphi_1}{\partial n} = -\frac{\partial \varphi_0}{\partial n} \quad \text{on } \partial B, \tag{8}$$

whereas at the actual free surface η we have

$$\frac{\partial \varphi_1}{\partial t} + \tfrac{1}{2}\nabla\varphi_1 \cdot \nabla\varphi_1 + \nabla\varphi_0 \cdot \nabla\varphi_1 + g\eta_1 = -\frac{\partial \varphi_0}{\partial t} - \tfrac{1}{2}\nabla\varphi_0 \cdot \nabla\varphi_0 - g\eta_0 \quad \text{on } S, \tag{9}$$

$$\frac{\partial \eta_1}{\partial t} + \frac{\partial \phi}{\partial x}\frac{\partial \eta_1}{\partial x} + \frac{\partial \phi}{\partial y}\frac{\partial \eta_1}{\partial y} = \frac{\partial \phi}{\partial z} - \frac{\partial \eta_0}{\partial t} - \frac{\partial \phi}{\partial x}\frac{\partial \eta_0}{\partial x} - \frac{\partial \phi}{\partial y}\frac{\partial \eta_0}{\partial y} \quad \text{on } S. \tag{10}$$

When the wave amplitude is estimated to be small enough, a reasonable description of the flow can be gained by the linearized version of (9) and (10):

$$\frac{\partial \varphi_1}{\partial t} + g\eta_1 = 0 \quad \text{on } z = 0, \tag{11}$$

$$\frac{\partial \eta_1}{\partial t} - \frac{\partial \varphi_1}{\partial z} = 0 \quad \text{on } z = 0. \tag{12}$$

Note that in the linear case the boundary conditions on the free surface are enforced on the undisturbed water plane $z = 0$ and, of course, only the first term in the Stokes wave is taken into account in the incident wave potential φ_0.

As stated before, the solution of the diffraction problem requires initial conditions for φ_1 and η_1.

2.2. Steady flow (wave resistance problem)

The computation of the steady wave pattern generated by a submerged or floating body moving with uniform forward speed U_∞ is one of the classic problems in naval hydrodynamics. The flow potential ϕ is typically computed by a unified free surface condition and the wave elevation is next obtained explicitly by the dynamic condition, whereas in the diffraction problem the kinematic and

dynamic conditions are generally implemented separately. In the fully non-linear case the free surface boundary conditions are

$$\left(\frac{\partial\phi}{\partial l}\right)^2\frac{\partial^2\phi}{\partial l^2}+g\frac{\partial\phi}{\partial z}=0 \quad \text{on } S, \tag{13}$$

$$z=\eta(x,y)=\frac{1}{2g}\left[U_\infty^2-\left(\frac{\partial\phi}{\partial l}\right)^2\right] \quad \text{on } S, \tag{14}$$

where l is a curvilinear abscissa defined along the streamline lying on the free surface.[10] In fact, in the steady case the free surface is an envelope of streamlines.

Linearized forms of the free surface conditions have also been considered in this work. In the Neumann–Kelvin problem the flow is linearized with respect to the free stream U_∞:

$$\frac{\partial^2\varphi_1}{\partial x^2}+\frac{g}{U_\infty^2}\frac{\partial\varphi_1}{\partial z}=-\frac{\partial^2\varphi_0}{\partial x^2} \quad \text{on } z=0, \tag{15}$$

$$z=\eta(x,y)=-\frac{U_\infty}{g}\left(\frac{\partial\varphi_0}{\partial x}+\frac{\partial\varphi_1}{\partial x}\right) \quad \text{on } z=0, \tag{16}$$

with

$$\phi(x,y,z)=U_\infty x+\varphi_0(x,y,z)+\varphi_1(x,y,z),$$

where φ_0 is the velocity potential due to the interaction between the free stream and the body (with $\partial\varphi_0/\partial z=0$ on $z=0$) and φ_1 is the velocity potential due to the interaction between the free stream, the body and the free surface. On the other hand, the Dawson formulation[9] implies the flow to be linearized with respect to the double model solution $\phi_0=U_\infty x+\varphi_0$:

$$\left(\frac{\partial\phi_0}{\partial l}\right)^2\frac{\partial^2\varphi_1}{\partial l^2}+2\frac{\partial\phi_0}{\partial l}\frac{\partial^2\phi_0}{\partial l^2}\frac{\partial\varphi_1}{\partial l}+g\frac{\partial\varphi_1}{\partial_z}=-\left(\frac{\partial\phi_0}{\partial l}\right)^2\frac{\partial^2\phi_0}{\partial l^2} \quad \text{on } z=0, \tag{17}$$

$$z=\eta(x,y)=\frac{1}{2g}\left[U_\infty^2-\left(\frac{\partial\phi_0}{\partial l}\right)^2-2\frac{\partial\phi_0}{\partial l}\frac{\partial\varphi_1}{\partial l}\right] \quad \text{on } z=0. \tag{18}$$

In this case, according to the linearization, the curvilinear abscissa l is defined on the local streamline of the basic flow lying on the symmetry plane $z=0$.

Of course, in the wave resistance problem no initial condition is to be applied, since the flow is steady. The uniqueness of the solution is then achieved by a radiation condition:

$$\lim_{x\to-\infty}\nabla\phi=U_\infty. \tag{19}$$

This condition implies that waves propagate only downstream, according to the dispersion properties of water waves free from surface tension.

3. INTEGRAL FORMULATION

The solution of the problems described in the previous section can be formulated in terms of the potential of single layer (giving rise to the classical boundary element method), i.e.

$$\varphi_1(P,t) = \int_{\partial D} \frac{\sigma(Q,t)}{|P-Q|}\, \mathrm{d}S, \tag{20}$$

where P is the field point and Q lies on the boundary of the fluid domain D. Desingularization consists of moving the source point Q outside the fluid domain. Moreover, the integral (20) has been replaced by a discrete summation of N isolated singularities located near the fluid domain boundary:

$$\varphi_1(P,t) = \sum_{i=1}^{N} \frac{\sigma_i(t)}{|P-Q_i|}, \tag{21}$$

the discrete source $\sigma_i(t)$ being placed in Q_i, which does not belong to ∂D.

The use of desingularized methods leads to certain mathematical difficulties. When the velocity potential is represented by a distribution of potential of simple layer over the actual boundary, the exact flow problem can be written as a Fredholm integral equation of the second kind. Solution existence and uniqueness theorems for this equation are well established. On the other hand, when the singularity sheet is moved away from the boundary, the integral equation of the second kind is replaced by one of the first kind, for which existence and uniqueness are not guaranteed, as manifested in the ill-conditioning of the resulting algebraic system if the desingularization distance is not properly chosen. In fact, desingularization increases the condition number of the resulting linear system. Webster[2] suggests the following considerations. By introducing proper error potentials, a sequence of potential problems leading to the exact flow can be conceived. Bearing in mind that as the grid is refined, the singularities approach the boundary with a suitable law, the singularity sheets related to these potentials would result in an onion-like layering, with each succeeding sheet closer to the exact boundary and each with a finer spacing. The limiting sheet lies on the actual boundary and is characterized by an infinitely refined mesh. Therefore, as the mesh size tends to zero, the non-singular formulation is consistent with the singular formulation and the same existence and uniqueness theorems can be used, as long as the desingularization distance is properly related to the mesh size.

4. ON THE CHOICE OF DESINGULARIZATION DISTANCE

This aspect is investigated by simple test problems in unbounded domains for which the exact solution is known and a simple discrete distribution of singularities can be imposed as a regular network of sources at the same height above the plane of the control points ($z=0$). The numerical error is then studied when the various parameters of the discretization are changed. Next the value of the source height is expressed by means of simple formulae as a function of the other discretization parameters.

However, the optimum value for the distance between the source point and the control point can change from case to case. This can be shown by a simple example, the same as used by Cao *et al.*[5] Consider the potential ψ induced on the plane $z=0$ by a dipole located at a certain submergence h. This potential can be obtained by a uniform distribution of sources on a horizontal plane and the solution of the Dirichlet problem

$$\sum_{k=1}^{N} \frac{\sigma_k}{|P-Q_k|} = \psi(P), \quad P = x, y, 0,$$

yields the source strength σ_k. Then, to check the effect of the source plane depth on the accuracy, the L_2-norm of the error E_2 with respect to the potential ψ can be evaluated on the normal derivative at the same collocation points:

$$E_2 = \sqrt{\left[\frac{1}{N}\sum_{i=1}^{N}\left(\sum_{k=1}^{N}\sigma_k \frac{\partial}{\partial z}\frac{1}{|P_i - Q_k|} - \frac{\partial \psi(P_i)}{\partial z}\right)^2\right]}, \quad P_i = x_i, y_i, 0.$$

As a result, in this case the optimum submergence for the singularity sheet, as the mesh is refined, approaches the dipole submergence h: this result could be misleading and cannot be extended to more general cases. Therefore, in order to obtain general enough information suitable to be extended to free surface problems, two examples of steady wavy flows have been examined. Then the correlation for the desingularization distance will be used for the numerical solution of more realistic flow configurations, yielding satisfactory results.

4.1. Steady free waves

The first problem studied consists of the numerical solution of a linearized free surface flow in an unbounded domain. The Neumann–Kelvin formulation outlined before is therefore implemented, but in the absence of any solid boundaries.

Hereinafter, all the quantities are considered non-dimensional, whereas dimensional variables are characterized by 'primes'. The exact dimensionless potential is

$$\varphi_1(x, y, z) = \frac{\varphi_1'}{U_\infty \lambda} = \frac{A'}{\lambda} e^{2\pi z/\lambda} \sin\left(2\Pi \frac{x'}{\lambda}\right) = A e^{2\pi z} \sin(2\pi x), \quad x, y \in [-\infty, \infty], \quad z \in [-\infty, 0], \tag{22}$$

where

$$\lambda = 2\pi U_\infty^2 / g \tag{23}$$

is the wavelength and A is a non-dimensional constant. The wave elevation is given by

$$\eta(x, y) = \frac{\eta'(x, y)}{\lambda} = -\frac{1}{2\pi}\frac{\partial \varphi_1(x, y, 0)}{\partial x} = -A\cos(2\pi x). \tag{24}$$

The numerical solution is obtained by solving the Dirichlet problem

$$\sum_{k=1}^{N} \frac{\sigma_k}{\sqrt{[(x_i - x_k)^2 + (y_i - y_k)^2 + Z_s^2]}} = A \sin(2\pi x_i), \quad i = 1, \ldots, N, \tag{25}$$

and the wave elevation η is computed by

$$\eta_i = -\sum_{k=1}^{N} \sigma_k = \frac{x_k - x_i}{[(x_i - x_k)^2 + (y_i - y_k)^2 + Z_s^2]^{3/2}}, \quad i = 1, \ldots, N, \tag{26}$$

The network of point sources is regular and is placed above a square region $2\lambda \times 2\lambda$ wide. Two cases have been considered: non-staggered-type grid (see Figure 1(a)) and staggered-type grid (see Figure 1(b)).

In Figure 2 the error E_2 is reported as a function of the non-dimensional source position $Z_s = Z_s'/\lambda$, where

$$E_2 = \sqrt{\left(\frac{1}{N}\sum_{i=1}^{N}[\eta_i + A\cos(2\pi x_i)]^2\right)}, \tag{27}$$

N being the number of control points in the non-staggered grid (four points per wavelength in each direction for the case shown in the figure). The reciprocal of the condition number is also reported in

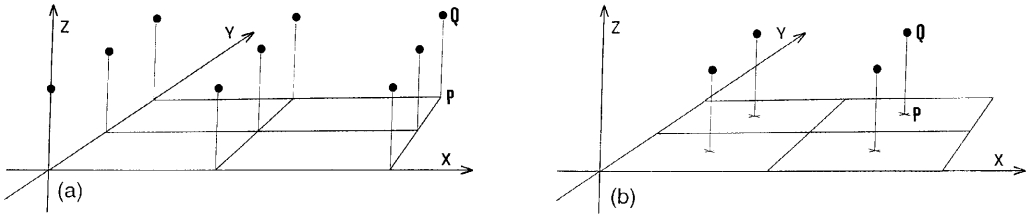

Figure 1. Sample grids: (a) non-staggered type; (b) staggered type

the same figure. It can be noted that the error has two local minima, one at $Z_s \approx 0{\cdot}5$ and the other at $Z_s \approx 2$. The latter minimum is slightly smaller than the former, but, conversely, the condition number is too large to be used in practical computations. Therefore the point source distance corresponding to the first local minimum is to be preferred.

In Figure 3 the error E_2 is reported, again as a function of Z_s, for 10 square element grids, the size ranging from $1/6$ to $1/15$ of the wavelength. The discretized domain has been held at $2\lambda \times 2\lambda$ wide in all cases. It can be observed that for all grids the numerical solutions show the same behaviour concerning the error.

In Figure 4 the optimum source distance from the free surface, $\tilde{Z}$, is plotted against the lateral grid dimension dy for each grid size dx (direction of wave propagation). The error E_2, as a function of the mesh size, is plotted in Figure 5(a) for square element staggered grids. Comparison with the method of Hess and Smith justifies the great interest of desingularization techniques. In fact, whereas the

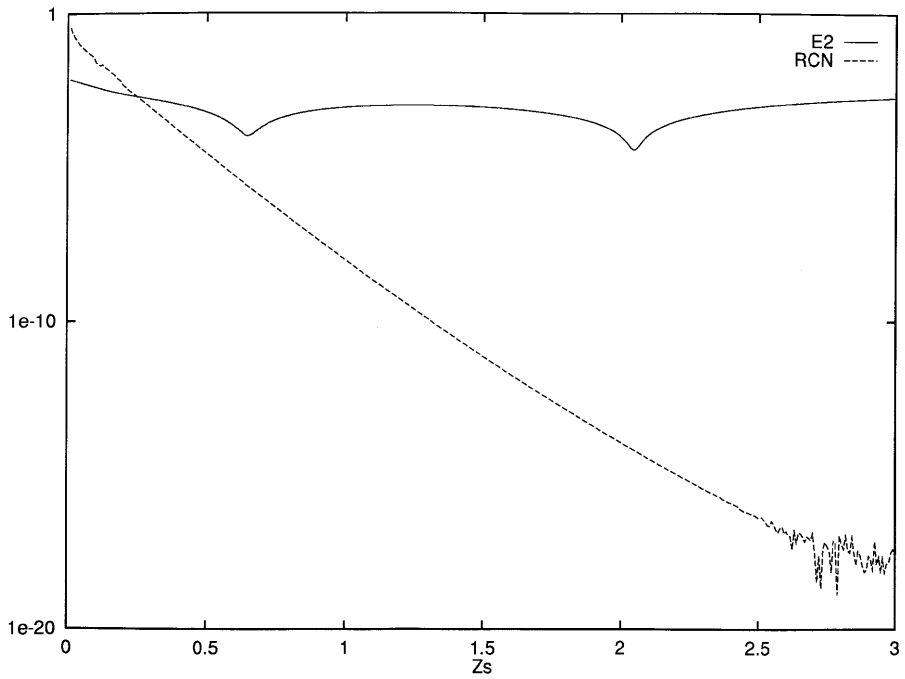

Figure 2. Numerical computation of a steady regular wave on a non-staggered grid: L_2-norm of error (E_2) and reciprocal of condition number (RCN) versus desingularization distance (Z_s). Discretization with four elements per wavelength

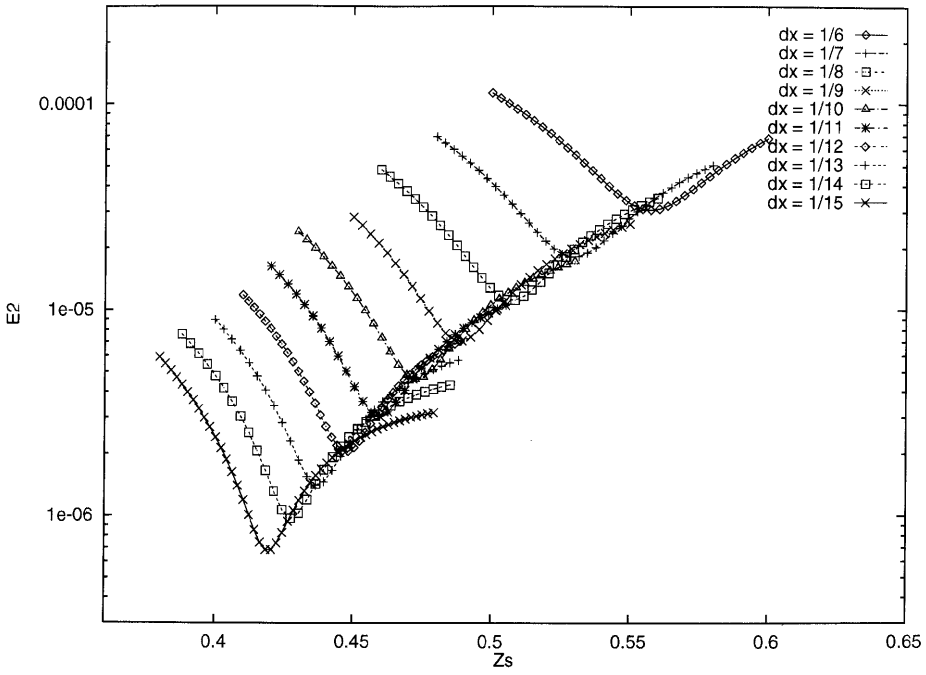

Figure 3. E_2 versus Z_s for 10 square element grids (non-staggered grid)

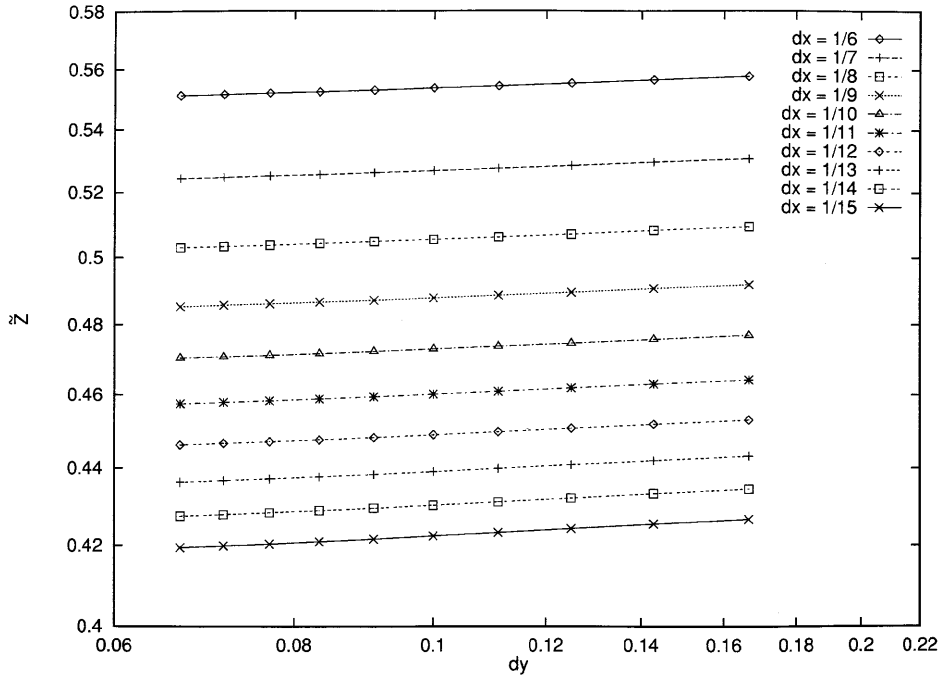

Figure 4. Optimum desingularization distance ($\tilde{Z}$) versus lateral grid size dy for various dx (non-staggered grid)

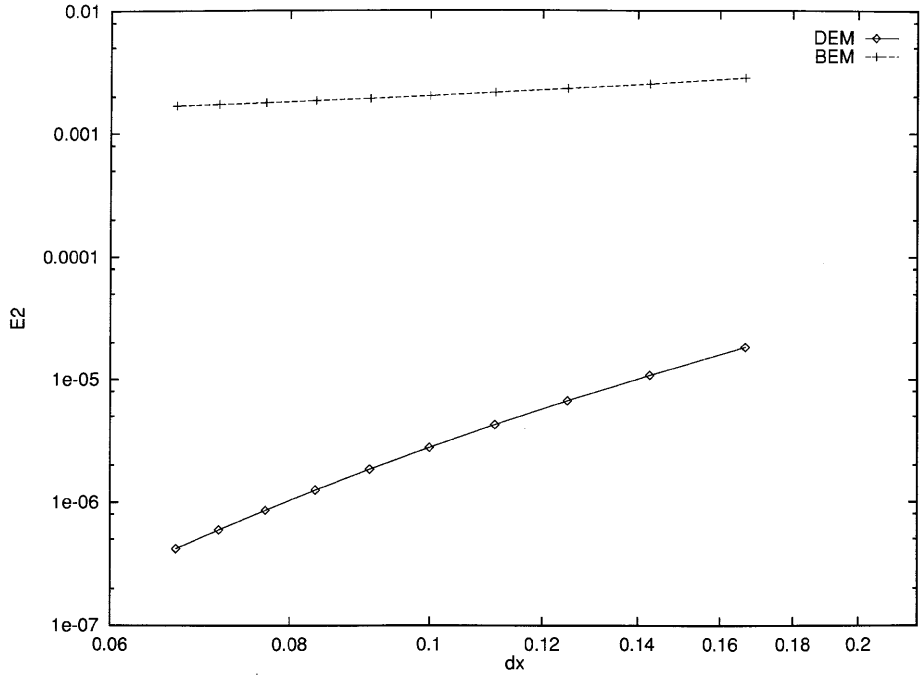

Figure 5(a). E_2 versus dx for desingularized method (DEM) and conventional panel method (BEM) for square element staggered grids

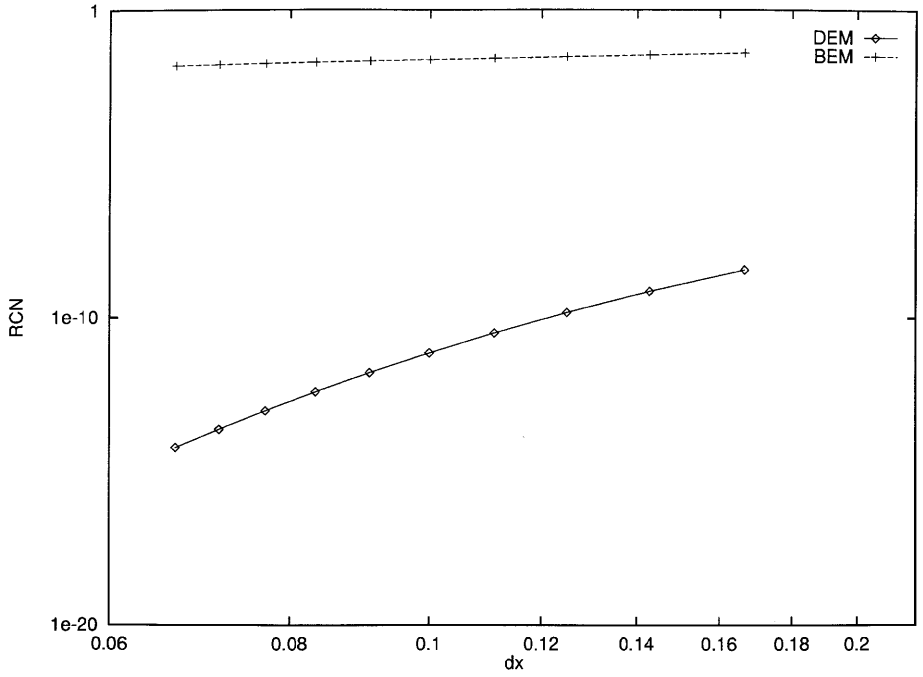

Figure 5(b). *RCN* versus dx for desingularized method (DEM) and conventional panel method (BEM) for square elements staggered grids

panel method exhibits a convergence approximately of order 0·6, the desingularized method shows a convergence nearly of the fourth order, though it is much simpler to implement and requires a significantly lower CPU time. On the other hand, Figure 5(b) shows the behaviour of the reciprocal of the condition number, again as a function of the mesh size. The best comment on this figure, when compared with the previous one, is a statement due to Cao *et al.*:[5] 'a poorly conditioned system does not necessarily imply an inaccurate solution'. Of course, all the results obtained in the present work have been computed in double precision, but it seems clear that grid refinement beyond a certain threshold can create some difficulties. In fact, the reciprocal of the condition number must be at least one order of magnitude higher than the round-off error, in order to obtain reliable solutions, also when direct solution methods for the resulting algebraic system are used, in particular when the system is large (e.g. a 5000×5000 matrix).

Moreover, in so far as Figure 5(a) shows grid refinement to produce very fast convergence to the exact solution, Figure 5(b) seems to suggest that in the limit a numerical solution does not exist, since the condition number rapidly tends to infinity. This result seems to be in contrast with the arguments outlined in Section 3, related to the consistency of the desingularized formulation with the singular one. On the other hand, it is worth noticing that the integral formulation cannot be replaced by a discrete distribution of singularities for much refined grids. Moreover, in the analysis carried out so far, the desingularization distance has been chosen in order to obtain the best accuracy in a practical range of the mesh size. It is reasonable to suppose that in the limit it is not possible to preserve the convergence rate previously shown, since, in fact, the singular formulation is less accurate than the non-singular one. Therefore, in so far as the mesh is much refined, the singularity sheet will approach the boundary with a different law in order to ensure consistency with the singular formulation.

The shape assumed by the curves of Figure 4 suggest that the use of the following expression for the optimum distance:

$$\tilde{Z} = k \, \mathrm{d}x^{\mu} \, \mathrm{d}y^{\nu}. \tag{28}$$

A similar expression is suggested by Cao *et al.*[5] In dimensional quantities, formula (28) reads

$$\tilde{Z}' = k\lambda^{1-\mu-\nu} \, \mathrm{d}x'^{\mu} \, \mathrm{d}y'^{\nu}. \tag{29}$$

The unknown constants k, μ and ν have been computed by a least squares fit, obtaining

$$k \approx 0{\cdot}969, \quad \mu \approx 0{\cdot}294, \quad \nu \approx 0{\cdot}016 \tag{30}$$

for the non-staggered grid, whereas for the staggered grid the following values are computed:

$$k \approx 1{\cdot}627, \quad \mu \approx 0{\cdot}453, \quad \nu \approx 0{\cdot}018. \tag{31}$$

For example, to give an idea of the difference between the correlations in these two cases, if we apply the values given by (30) on a staggered grid with $\mathrm{d}x = \mathrm{d}y = 1/6$, we obtain $\tilde{Z} \approx 0{\cdot}556$ and $E_2 \approx 2 \times 10^{-4}$, instead of the proper values $\tilde{Z} \approx 0{\cdot}711$ and $E_2 \approx 2 \times 10^{-5}$ obtained by the use of (31) in the integral equation. This difference, though seemingly meaningless for practical applications (in both cases the solution is very accurate), is nevertheless significant.

Formula (28) has next been used for the vertical positioning of sources in non-uniform grids coarsened towards the boundaries of the truncated domain. In particular, the same computations related to the steady plane wave have been performed on two types of grids: in the first case the ratio between the sizes of the largest element and the smallest one is equal to 1·875, whereas in the second case this ratio is equal to 2·5.

The computation of such a regular flow field does not require, of course, the use of a stretched grid; this test case has been carried out in order to check the numerical behaviour of the method in non-uniform geometries. However, similar situations occur in applications; in fact, in the far field the mesh is typically coarsened, in particular when a polar grid is used.

Figure 6(a) shows the error E_2 as a function of the number of elements for the panel method in the case of uniform and non-uniform grids. As seems reasonable, the convergence behaviour is very similar in the three cases: in fact, in stretched grids the higher accuracy in the fine mesh region is more or less balanced by the lower accuracy in the coarse mesh region. The small difference is probably due to the different effect of truncation in the three cases.

Figure 6(b) shows the error E_2 as a function of the number of elements for the desingularized method. The broken curves are obtained by the vertical positioning of singularities according to (28) and (31), whereas the dotted and chain curves refer to the distribution of sources on a horizontal plane whose height decreases as the number of elements increases, as usual. These results suggest that a uniform network is always preferable, also because the ill-conditioning of the resulting linear system becomes worse in non-uniform discretizations. However, as long as a stretched grid is inevitable, the arrangement of singularities on a horizontal plane is to be preferred. The oscillations in the curve related to the second stretched grid (sources positioned according to local mesh size) are due to ill-conditioning: in this case the reciprocal of the condition number reduces beneath the threshold of the round-off error.

In the present work the numerical applications to practical cases have therefore been performed using uniformly spaced grids.

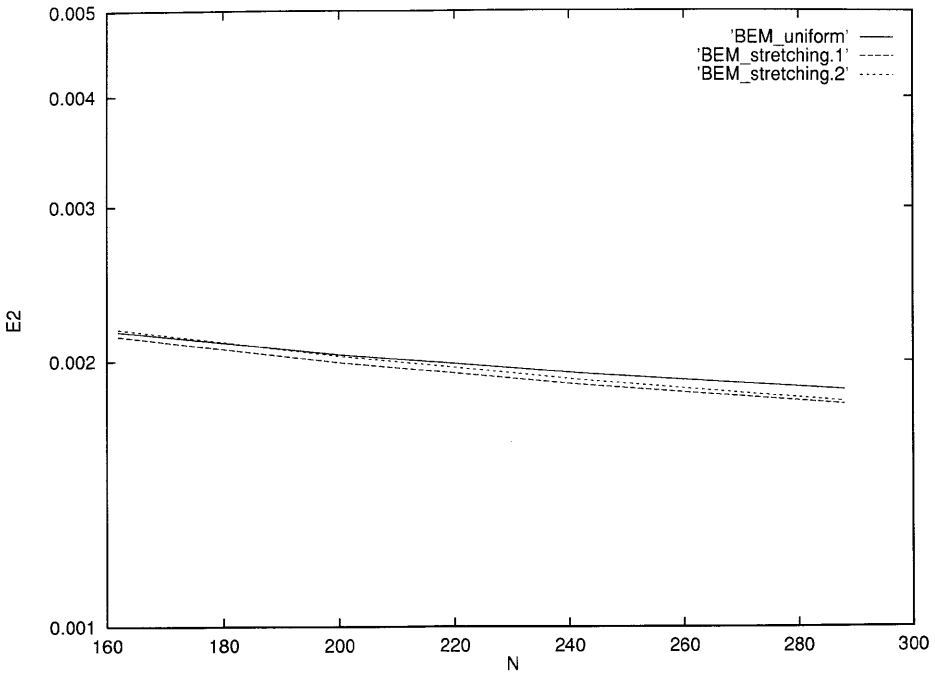

Figure 6(a). E_2 versus number of elements in uniform and non-uniform staggered grids for conventional panel method

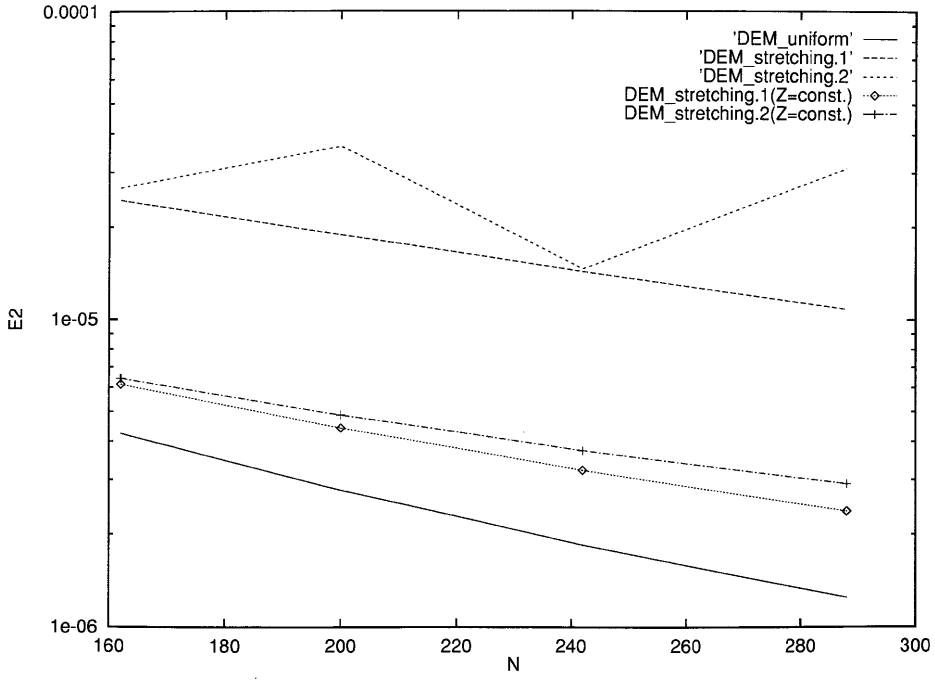

Figure 6(b). E_2 versus number of elements in uniform and non-uniform staggered grids for desingularized method

4.2. *Steady waves past a submerged dipole*

The analytical solution for the wave pattern generated by the potential flow past a sphere located at $(0, 0, -h)$ is given by[11]

$$\eta(x,y) = \frac{h}{8(r^2+h^2)^{3/2}} + \frac{1}{8\pi Fr^2}\int_{-\pi/2}^{\pi/2} \mathrm{d}\alpha \int_0^{\infty} \frac{\cos(mh) + m\sin(mh)\cos^2\alpha}{\cos^4(\alpha m^2) + 1/Fr^4} \mathrm{e}^{-mr|\cos(\alpha-\theta)|} m\,\mathrm{d}m + \frac{1}{4Fr^4}\int_{-\pi/2}^{\theta-\pi/2} \sec^4\alpha \sin\left(\frac{r}{Fr^2}\cos(\alpha-\theta)\sec^2\alpha\right)\mathrm{e}^{-(h/Fr^2)\sec^2\alpha}\,\mathrm{d}\alpha, \tag{32}$$

where $Fr = U_\infty/\sqrt{(gL)}$ is the Froude number related to the diameter L of the submerged sphere, $r = \sqrt{(x^2+y^2)}$ and $\theta = \tan^{-1}(y/x)$. The numerical solution is obtained by the discrete form of (15) and (16). In this case, φ_0 is the potential of the dipole and its image:

$$\varphi_0(x,y,z) = M\left(\frac{x}{[x^2+y^2+(z+h)^2]^{3/2}} + \frac{x}{[x^2+y^2+(z-h)^2]^{3/2}}\right).$$

The dipole strength M is $U_\infty L^3/16$. The convective term $\partial^2\varphi_1/\partial x^2$ which appears in the unified free surface condition (15) is implemented by analytical derivation, whereas the radiation condition is satisfied by upstream shift of the collocation points[10,12] (or by downstream shift of the source locations). Moreover, according to the analytical model, the potential φ_1 does not fulfil the impermeability condition on the sphere surface.

The distribution of sources of strength σ_i lies above the free surface, at a distance given by the correlation (28), calibrated for the staggered-type grid.

In Figure 7 the numerical results are compared with the analytical solution (32) ($h = 0{\cdot}7, Fr = 0{\cdot}4$). The computational domain, discretized by a staggered-type grid, has been taken as 3·5 wavelengths long (two downstream and 1·5 upstream) and two wavelengths wide; 224 elements have been used, with every wavelength described by eight nodes. Figure 7(a) shows a comparison between the contour lines of the wave pattern: the lower part is the analytical solution

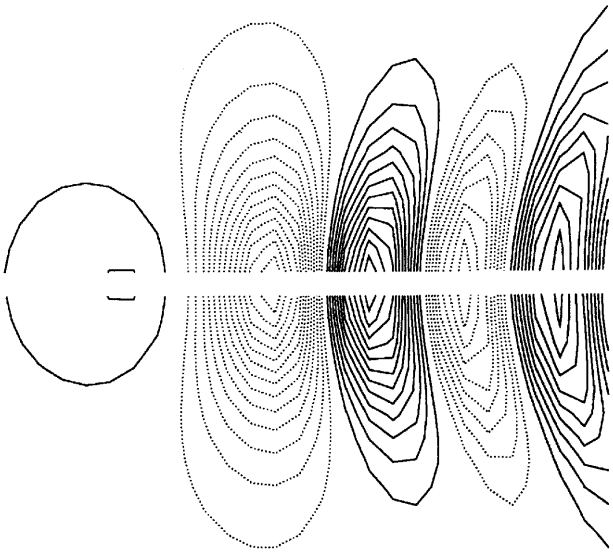

Figure 7(a). Steady waves past a submerged dipole: comparison between analytical and numerical solutions (Froude number 0·4, depth 0·7); contour lines of analytical solution (bottom half) and numerical solution obtained by desingularized method (top half). Levels $-0{\cdot}139,\ldots,+0{\cdot}127$ (0·01)

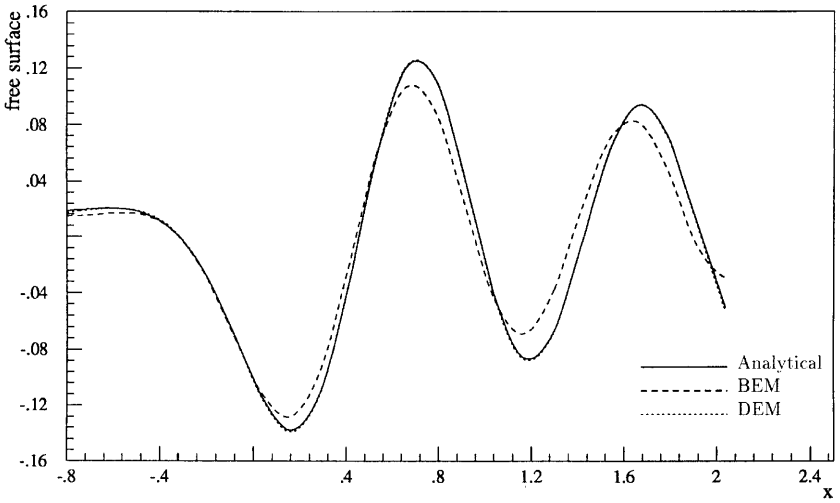

Figure 7(b). As in Figure 7(a): comparison between analytical and numerical solutions at longitudinal mid·section

and the upper part is the numerical solution. In Figure 7(b), longitudinal mid-sections of the wave pattern are depicted. In both cases the good accuracy of the desingularized method is apparent, in particular when compared with the method of Hess and Smith.

5. NUMERICAL APPLICATIONS

In the numerical examples the surface of the solid body has been discretized by N_B quadrilateral flat panels on which the source strength is piecewise constant.[13] On the free surface the boundary integral is approximated by a distribution of N_S sources placed at a fixed distance above the boundary, following the criteria outlined in the previous section.

In the non-linear problem the singularities are moved vertically at each time step (or, in the steady case, at each iteration) following the wave elevation, according to the correlations obtained previously. Cao *et al.*[5] suggest the singularities to be moved in a direction normal to the free surface: this could be important for the simulation of rather steep waves.

5.1. Unsteady flow (diffraction problem)

The first numerical example studied is concerned with the wave diffraction of regular waves around a fixed obstacle in finite depth waters. The presence of the bottom is taken into account by means of the method of images. The representation of the perturbation potential can be therefore summarized in the formula

$$\varphi_1(P) = \sum_{j=1}^{N_B} \sigma_j \left(\int_{\partial B_j} G(P, Q)\, \mathrm{d}S + \int_{\partial \tilde{B}_j} G(P, Q)\, \mathrm{d}S \right) + \sum_{k=1}^{N_S} \sigma_k [G(P, Q_k) + G(P, \tilde{Q}_k)], \tag{33}$$

where ∂B_j is the jth panel on the surface of the obstacle, σ_j is the (constant) source density on it, $\partial \tilde{B}_j$ is the mirror image of ∂B_j with respect to the bottom, Q_k is the position of the kth source above the free surface, σ_j is the source strength at Q_k and $\tilde{Q}_k$ is the image of Q_k.

In the unsteady numerical simulation the solution is updated from t^n to $t^n + \Delta t = t^{n+1}$ by means of the classical fourth-order Runge–Kutta scheme. Each intermediate stage of the Runge–Kutta algorithm is computed as follows:

1. Given the potential φ_1 and its derivatives on $\partial B \cup S$ at the previous stage, the dynamic and kinematic boundary conditions (9) and (10) (or (11) and (12) in the linear case) are used to update the flow field at the free surface.
2. The new values of φ_1 in the N_S collocation points on the free surface and the Neumann boundary condition at the N_B collocation points on the body surface give rise to $N_B + N_S$ linear conditions relating the $N_B + N_S$ unknowns σ_j and σ_k. The resulting linear system is solved by LU factorization of the coefficient matrix.
3. The new source strengths σ_j and σ_k yield the values of φ_1 and its derivatives on $\partial B \cup S$ for the next Runge–Kutta stage.

An important aspect is the behaviour of the numerical model far from the body; in fact, since the boundary extends to infinity, a far-field condition is required in order to avoid unphysical reflection of the outgoing waves at the truncation of the computational domain. These reflected waves, if not damped, can remarkably affect the wave field around the obstacle, as will be shown later. In the present work this problem is solved by means of the damping layer suggested by Baker *et al.*:[14] the term $-\varepsilon\varphi_1$ is added to the right-hand side of the dynamic boundary condition (9) (or (11) in the linear case), whereas the term $-\varepsilon\eta_1$ is introduced on the right-hand side of the kinematic boundary

condition (10) (or (12) in the linear case), namely

$$\text{LHS of}\left\{\begin{array}{c}\text{eq. (9)}\\ \text{eq. (11)}\end{array}\right\} = \text{RHS of}\left\{\begin{array}{c}\text{eq. (9)}\\ \text{eq. (11)}\end{array}\right\} - \varepsilon\varphi_1, \tag{34}$$

$$\text{LHS of}\left\{\begin{array}{c}\text{eq. (10)}\\ \text{eq. (12)}\end{array}\right\} = \text{RHS of}\left\{\begin{array}{c}\text{eq. (10)}\\ \text{eq. (12)}\end{array}\right\} - \varepsilon\eta_1, \tag{35}$$

where ε is a coefficient depending on the distance from the obstacle. In the problem studied in this paper, it has the expression

$$\varepsilon = \begin{cases} 0, & r < R_0, \\ \varepsilon_0\left(\dfrac{r - R_0}{R_1 - R_0}\right)^2, & R_0 \leqslant r \leqslant R_1, \\ \varepsilon_0, & r > R_1, \end{cases} \tag{36}$$

where ε_0 is a fixed coefficient (typically $\varepsilon_0 = O(1)$ in the calculations performed), $r = \sqrt{(x^2 + y^2)}$ is the distance from the origin and R_0 and $R_1 > R_0$ are two real numbers chosen on the basis of numerical experience ($R_1 - R_0 = O(\lambda)$).

In the far field these terms act like a damper only on the perturbation potential φ_1 and on the wave height η_1, while the assigned basis flow is not affected. As previously mentioned, this is one of the major advantages of the decomposition (6).

In the numerical example the wave diffraction around a simple-shaped shoal is computed and the results are compared with experimental data.[15] The geometry of the bottom is given by (see Figure 8)

$$z = \begin{cases} (h_{\mathrm{M}} - h_{\mathrm{m}})(r/R_{\mathrm{S}})^2 + h_{\mathrm{m}}, & r < R_{\mathrm{S}}, \\ h_{\mathrm{M}}, & r \geqslant R_{\mathrm{S}}, \end{cases} \tag{37}$$

where h_{M} and h_{m} are the maximum and minimum depths respectively and R_{S} is the radial extension of the shoal. Moreover, in the case studied, $R_{\mathrm{S}}/\lambda = 2$, $h_{\mathrm{M}}/\lambda = 0{\cdot}375$ and $h_{\mathrm{m}}/\lambda = 0{\cdot}125$, where λ is the wavelength.

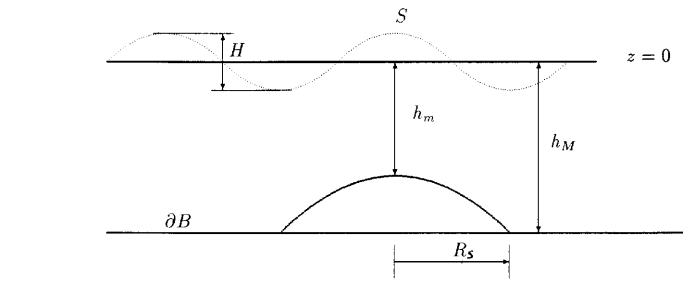

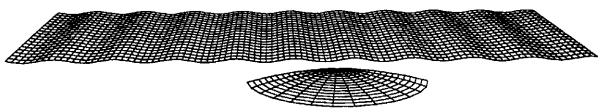

Figure 8. Diffraction around a shoal: top, sketch of problem; bottom, sample grid

In the computations the shoal is discretized with 224 panels, whereas a suitable grid for the free surface has been chosen by means of numerical experiments. In Figure 9 the ratio of the linear diffracted wave amplitude to the incident wave amplitude at the transverse section located at $x = R_S$ is plotted. The computation has been performed on four grids containing 36×9, 47×11, 70×16 and 93×21 elements. For all cases the discretized free surface is $11{\cdot}5\lambda$ long (5.2λ in the upwave region and $6{\cdot}3\lambda$ in the downwave region) and $3{\cdot}75\lambda$ wide. Moreover, for all the grids the ratio dy/dx between the mesh sizes in the transverse and longitudinal directions equal to 1·5. The behaviour shown in Figure 9 indicate that the convergence is very fast and the computations can be performed with the third grid (six elements per wavelength).

In Figure 10 the linear results are compared with the non-linear ones, computed with the same grid, and with experimental data[15] at the same transverse section and at another one located $R_S/2$ downwave. The incident wave steepness is $2\pi H/\lambda = 0{\cdot}1$.

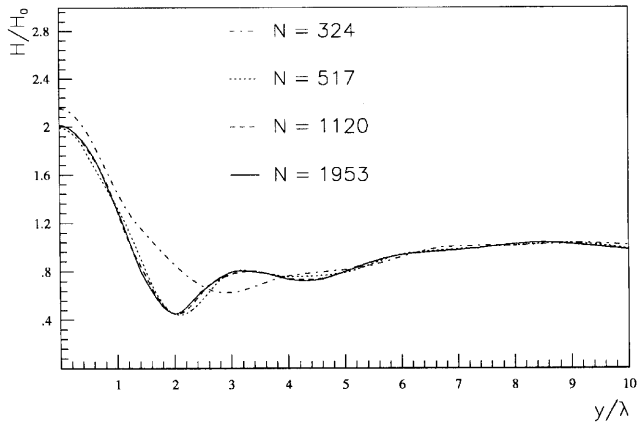

Figure 9. As in Figure 8: grid dependence test in a transverse section located downwave, above end of shoal

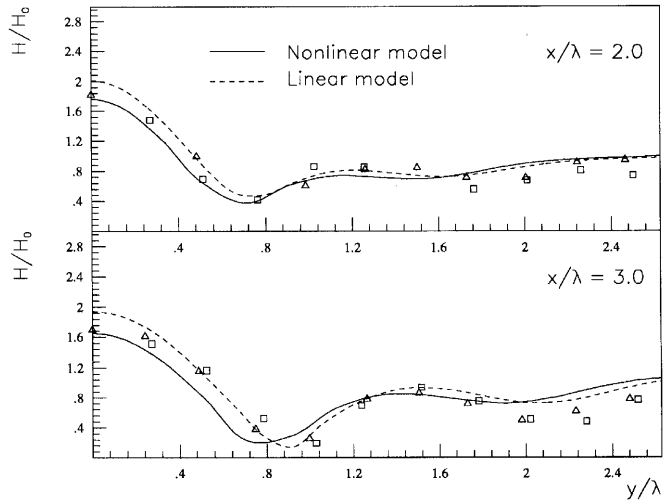

Figure 10. As in Figure 8: comparison between numerical results and experimental data (□, left side; △, right side) at two transverse sections located downwave

Above the top of the shoal, in the middle of the fluid domain, the non-linear model gives a better prediction of the wave height than the linear one, whereas, departing from the obstacle, the linear and non-linear models give similar results and both show a reasonable agreement with experimental data.

In Figure 11, finally the importance of the damping layer can be observed. In the longitudinal mid-section the envelope of the wave elevation η_1 is shown in the presence and absence of the 'numerical beach'. Whereas in the computations with the damping layer the envelope, after the initial transient, becomes steady and regularly shaped, in the other case it is evident how reflected waves significantly affect the fluid domain. In the figure the damping coefficient is not plotted to scale for the sake of clarity. In the computations the damping layer has been used with the following coefficients:

$$R_0 = 2{\cdot}5\lambda, \quad R_1 - R_0 = \lambda, \quad \varepsilon_0 = 0{\cdot}4.$$

The diffraction problem around the parabolic shoal was also studied in a previous work,[8] yielding more or less similar results, but in the present paper the computational cost has been significantly reduced (six elements per wavelength versus 14) by means of the systematic analysis concerning the desingularization distance.

5.2. *Steady flow (wave resistance problem)*

In the diffraction problem the potential φ_0 is a known function, whereas in the wave resistance problem the double model potential is computed, as the first step in the numerical procedure, by the impermeability condition on the body

$$\frac{\partial \varphi_0}{\partial n} = -\vec{U}_\infty \cdot \vec{n}, \tag{38}$$

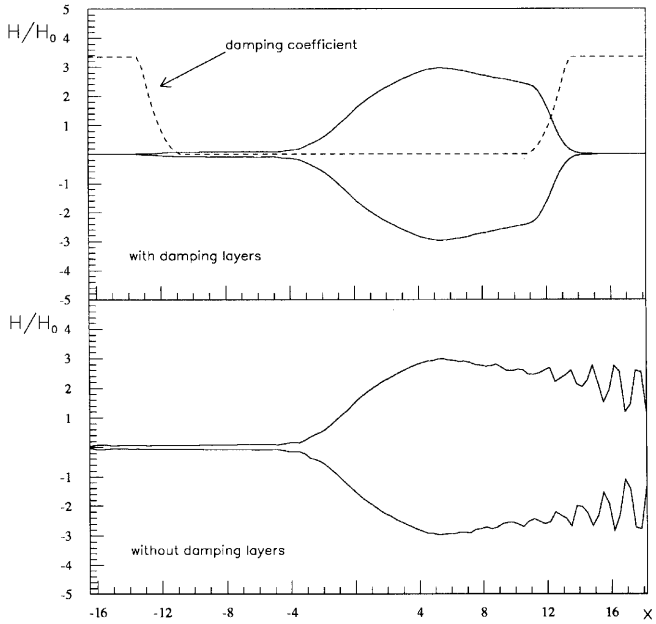

Figure 11. As in Figure 8: effect of damping layer

where

$$\varphi_0(P) = \sum_{j=1}^{N_B} \sigma_{0j} \left(\int_{\partial B_j} G(P, Q)\, \mathrm{d}S + \int_{\partial \bar{B}_j} G(P, Q)\, \mathrm{d}S \right), \tag{39}$$

$\partial \bar{B}_j$ being the mirror image of ∂B_j with respect to the unperturbed free surface ($z = 0$). In this case the perturbation potential φ_1 has the expression

$$\varphi_1(P) = \sum_{j=1}^{N_B} \sigma_j \int_{\partial B_j} G(P, Q)\, \mathrm{d}S + \sum_{k=1}^{N_S} \sigma_k G(P, Q_k), \tag{40}$$

since these numerical examples are concerned with deep waters.

Linear and fully non-linear conditions at the free boundary have been considered. For the linear problem the Dawson formulation has been implemented,[9] whereas the non-linear problem is solved by a successive linearization iterative procedure. At every step a linear problem is solved. The potential $\phi(x, y, z)$ is split into two terms:

$$\phi^{n+1} = \phi^n + \varphi_1. \tag{41}$$

In this decomposition the basic flow is the solution at the previous step. Therefore the nth step consists of the solution of equation (17), linearized around the free surface flow computed at the previous step:

$$\left(\frac{\partial \phi^n}{\partial l}\right)^2 \frac{\partial^2 \varphi_1}{\partial l^2} + 2 \frac{\partial \phi^n}{\partial l} \frac{\partial^2 \phi^n}{\partial l^2} \frac{\partial \varphi_1}{\partial l} + \frac{1}{Fr^2} \frac{\partial \varphi_1}{\partial z} = -\left(\frac{\partial \phi^n}{\partial l}\right)^2 \frac{\partial^2 \phi^n}{\partial l^2} - \frac{1}{Fr^2} \frac{\partial \phi^n}{\partial z}. \tag{42}$$

This iterative algorithm, similar to others proposed in the literature,[3,7] is more efficient than the method developed in a previous work[10] based on a double cycle of iterations.

As in the diffraction problem, in the non-linear case the sources are moved vertically, within the iterative procedure, according to (28) and (31), since staggered-type grids have been used.

The method has been implemented for the computation of the wave pattern generated by the steady motion of two submerged bodies of revolution (Figure 12):

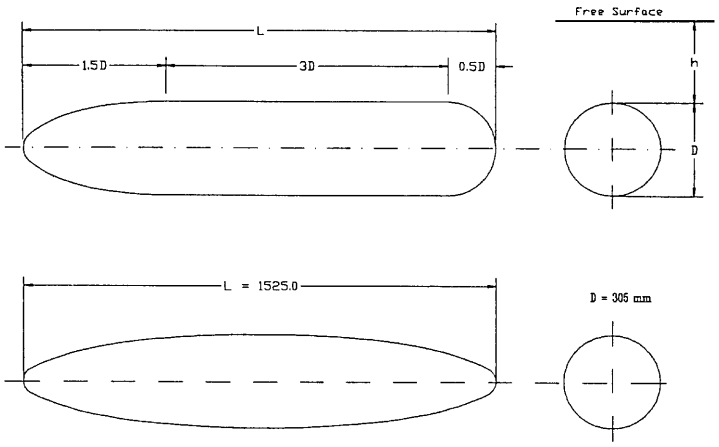

Figure 12. Bodies of revolution considered in wave resistance problem

(a) a circular cylinder with a half-sphere-shaped 'bow' and the 'stern' constituted by a half-prolate spheroid
(b) a prolate spheroid.

All the computations have been carried out on a uniform 32×9 grid with square elements, extending $1{\cdot}2L$ upstream, $2{\cdot}4L$ downstream and L sideways. Each wavelength has been discretized by 11 elements. The linear results have been obtained by the Dawson formulation. In Figure 13(a) the free surface contour lines are depicted in the linear case (bottom half) and in the non-linear case (top half). The wave steepening as well as the wavelength shortening, typical of non-linear waves, can be recognized. The results have also been compared with some experimental data obtained at the University of Trieste.[16] Figure 13(b) shows three longitudinal sections of the free surface; the improvement of the non-linear results with respect to the linear ones is apparent.

Finally, in Figures 14(a) and 14(b) the same results obtained for the prolate spheroid are depicted. Also in this case the non-linear results show rather good agreement with the experimental data.

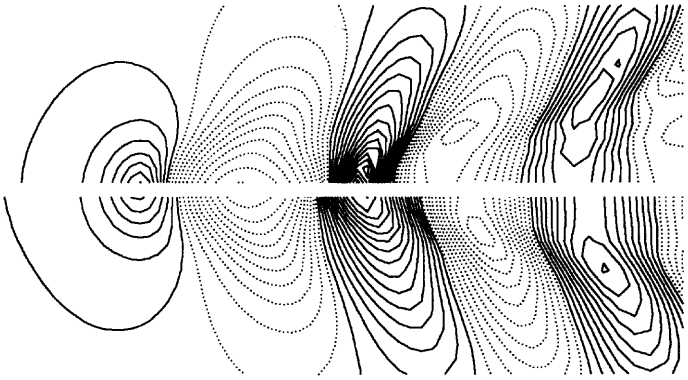

Figure 13(a). Steady waves past a submerged cylinder: comparison between linear (bottom half) and non-linear (top half) methods. Linear solution levels $-0{\cdot}040,\ldots,+0{\cdot}057$ (0·004). Non-linear solution levels $-0{\cdot}042,\ldots,+0{\cdot}062$ (0·004)

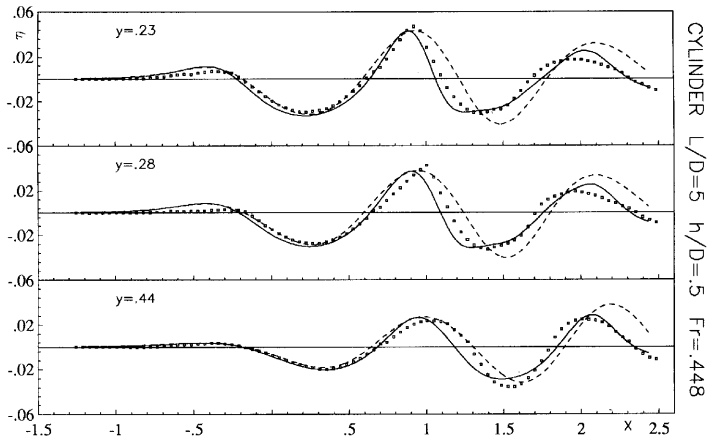

Figure 13(b). As in Figure 13(a): comparison between experimental data and numerical solution at longitudinal sections

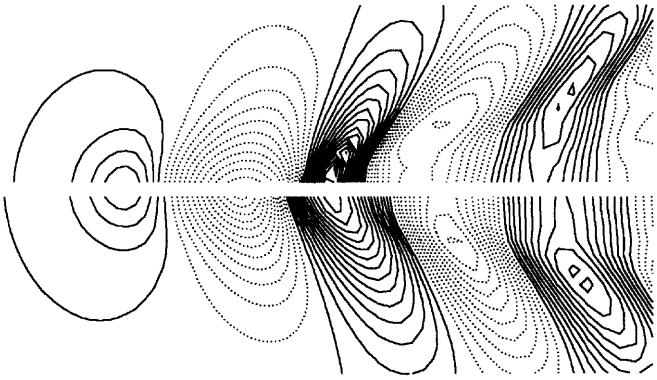

Figure 14(a). Steady waves past a submerged prolate spheroid: comparison between linear (bottom half) and non-linear (top half) methods. Linear solution levels $-0{\cdot}049,\ldots,+0{\cdot}055$ (0·004). Non-linear solution levels $-0{\cdot}046,\ldots,+0{\cdot}060$ (0·004)

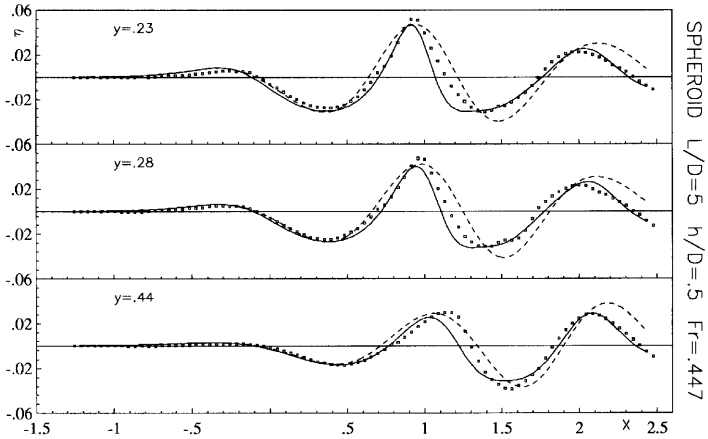

Figure 14(b). As in Figure 14(a): comparison between experimental data and numerical solution at longitudinal sections

6. CONCLUSIONS

Some free surface potential flow computations were performed making use of the concept of boundary integral desingularization. The properties of numerical algorithms based on the desingularized boundary integral formulation were analysed: simple test cases were studied showing the high accuracy typical of this kind of method (about fourth-order). The main contribution of this work is to specify the criteria related to the choice of the optimum desingularization distance, which could be crucial for the efficiency of desingularized methods. The optimum value for this distance was then given, by simple correlations, as a function of the mesh size.

In the numerical examples, concerned with wave diffraction around fixed obstacles and wave resistance of submerged bodies, grid dependence tests and comparisons with experimental data show a very satisfactory numerical behaviour of the desingularized element method.

On the other hand, the results obtained for non-uniform grids seem to suggest that the desingularized method, formulated in terms of point sources, is not so suitable for complicated geometries, for which strongly deformed grids are needed. This problem will be the subject of future work.

ACKNOWLEDGEMENTS

The author wishes to acknowledge A. Di Mascio and M. Landrini for useful comments and criticism during the whole research. This work was supported by Italian Ministero dei Transporti e della Navigazione in the frame of Programma Ricerche INSEAN 1994–96.

REFERENCES

1. C. Patterson and M. A. Sheikh, in C. A. Brebbia (ed.), *Boundary Element Methods*, Springer, New York, 1981.
2. W. C. Webster, 'The flow about arbitrary, three-dimensional smooth bodies', *J. Ship Res.*, **19**, 206–218 (1975).
3. G. Jensen, H. Soding and Z. X. Mi, 'Rankine source method for numerical solutions of the steady wave resistance problem', *Proc. XVI Symp. on Naval Hydrodynamics*, Berkeley, CA, 1986, pp. 575–582.
4. W. W. Schultz and S. W. Hong, 'Solution of potential problems using an overdetermined complex boundary integral method', *J. Comput. Phys.*, **84**, 919–990 (1989).
5. Y. Cao, W. W. Schultz and R. F. Beck, 'Three-dimensional desingularised boundary integral method for potential problems', *Int. j. numer. methods fluids*, **12**, 785–803 (1991).
6. H. C. Raven, 'Nonlinear ship wave calculations using the RAPID method', *Proc. Int. Conf. on Numerical Ship Hydrodynamics*, Iowa City, IA, 1993, pp. 95–118.
7. D. Scullen and E. O. Tuck, 'Non-linear free-surface flow computation for submerged cylinders', *J. Ship Res.*, **39**, 185–193 (1995).
8. F. Lalli, A. Di Mascio and M. Landrini, 'Nonlinear diffraction effects around a surface-piercing structure', *Int. J. Offshore Polar Eng.*, **6**, 104–111 (1996).
9. C. W. Dawson, 'A practical computer method for solving ship-wave problems', *Proc. 2nd Int. Conf. on Numerical Ship Hydrodynamics*, Berkeley, CA, 1977.
10. P. Bassanini, U. Bulgarelli, E. Campana and F. Lalli, 'The wave resistance problem in a boundary integral formulation', *Surv. Math. Ind.*, **4**, 151–194 (1994).
11. T. H. Havelock, 'The wave pattern of a doublet in a stream', *Proc. R. Soc. Lond. A*, **121**, 288–299 (1928).
12. P. S. Jensen, 'On the numerical radiation condition in the steady-state ship wave problem', *J. Ship Res.*, **31**, 14–22 (1987).
13. J. L. Hess and A. M. O. Smith, 'Calculation of potential flows around arbitrary bodies', *Prog. Aeronaut. Sci.*, **8**, 1–139 (1966).
14. G. R. Baker, D. I. Meiron and S. A. Orszag, 'Generalized vortex methods for free-surface flow problems', *J. Fluid Mech.*, **123**, 477–501 (1982).
15. Y. Ito and K. Tanimoto, 'A method of numerical analysis of wave propagation. Application to wave diffraction and refraction', *Proc. Coastal Engineering Conf.*, 1972.
16. F. Lalli, R. Marcolini, R. Penna and I. Zotti, 'Experimental and numerical methodologies in ship design, *Tecnica Italiana*, **2**, 71–87 (1995).

